Low-dose CT image super-resolution network with dual-guidance feature distillation and dual-path content communication

Jianning Chi, Zhiyi Sun, Tianli Zhao, Huan Wang, Xiaosheng Yu, and Chengdong Wu

Faculty of Robot Science and Engineering, Northeastern University, Shenyang, China
chijianning@mail.neu.edu.cn

Abstract. Low-dose computer tomography (LDCT) has been widely used in medical diagnosis yet suffered from spatial resolution loss and artifacts. Numerous methods have been proposed to deal with those issues, but there still exists drawbacks: (1) convolution without guidance causes essential information not highlighted; (2) features with fixed-resolution lose the attention to multi-scale information; (3) single super-resolution module fails to balance details reconstruction and noise removal. Therefore, we propose an LDCT image super-resolution network consisting of a dual-guidance feature distillation backbone for elaborate visual feature extraction, and a dual-path content communication head for artifacts-free and details-clear CT reconstruction. Specifically, the dual-guidance feature distillation backbone is composed of a dual-guidance fusion module (DGFM) and a sampling attention block (SAB). The DGFM guides the network to concentrate the feature representation of the 3D inter-slice information in the region of interest (ROI) by introducing the average CT image and segmentation mask as complements of the original LDCT input. Meanwhile, the elaborate SAB utilizes the essential multi-scale features to capture visual information more relative to edges. The dual-path reconstruction architecture introduces the denoising head before and after the super-resolution (SR) head in each path to suppress residual artifacts, respectively. Furthermore, the heads with the same function share the parameters so as to efficiently improve the reconstruction performance by reducing the amount of parameters. The experiments compared with 6 state-of-the-art methods on 2 public datasets prove the superiority of our method. The code is made available at https://github.com/neu-szy/dual-guidance_LDCT_SR.

Keywords: Low-dose computed tomography · Image denoising · Image super-resolution · Deep learning.

1 Introduction

Following the "as low as reasonably achievable" (ALARA) principle [22], low-dose computer tomography (LDCT) has been widely used in various medical

applications, for example, clinical diagnosis [18] and cancer screening [28]. To balance the high image quality and low radiation damage compared to normal-dose CT (NDCT), numerous algorithms have been proposed for LDCT super-resolution [3,4].

In the past decades, image post-processing techniques attracted much attention from researchers because they did not rely on the vendor-specific parameters [2] like iterative reconstruction algorithms [1,23] and could be easily applied to current CT workflows [29]. Image post-processing super-resolution (SR) methods could be divided into 3 categories: interpolated-based methods [16,25], model-based methods [13,14,24,26] and learning-based methods [7,8,9,17]. Interpolated-based methods could recover clear results in those flattened regions but failed to reconstruct detailed textures because they equally recover information with different frequencies. And model-based methods often involved time-consuming optimization processes and degraded quickly when image statistics were biased from the image prior [6].

With the development of deep learning (DL), various learning-based methods have been proposed, such as EDSR [20], RCAN [31], and SwinIR [19]. Those methods optimized their trainable parameters by pre-degraded low-resolution (LR) and high-resolution (HR) pairs to build a robust model with generalization and finally reconstruct SR images. However, they were designed for known degradation (for example bicubic degradation) and failed to deal with more complex and unknown degradation processes (such as LDCT degradation). Facing more complex degradation processes, blind SR methods have attracted attention. Huang et al. [11] introduced a deep alternating network (DAN) which estimated the degradation kernels and corrected those kernels iteratively and reconstructed results following the inverse process of the estimated degradation. More recently, aiming at improving the quality of medical images further, Huang et al. [12] first composited degradation model proposed for radiographs and proposed attention denoising super-resolution generative adversarial network (AID-SRGAN) which could denoise and super-resolve radiographs simultaneously. To accurately reconstruct HR CT images from LR CT images, Hou et al. [10] proposed a dual-channel joint learning framework which could process the denoising reconstruction and SR reconstruction in parallel.

The aforementioned methods still have drawbacks: (1) They treated the regions of interest (ROI) and regions of uninterest equally, resulting in the extra cost in computing source and inefficient use for hierarchical features. (2) Most of them extracted the features with a fixed resolution, failing to effectively leverage multi-scale features which are essential to image restoration task [27,32]. (3) They connected the SR task and the LDCT denoising task stiffly, leading to smooth texture, residual artifacts and unclear edges.

To deal with those issues, as shown in Fig. 1(a), we propose an LDCT image SR network with dual-guidance feature distillation and dual-path content communication. Our contributions are as follows: (1) We design a dual-guidance fusion module (DGFM) which could fuse the 3D CT information and ROI guidance by mutual attention to make full use of CT features and reconstruct clearer

textures and sharper edges. (2) We propose a sampling attention block (SAB) which consists of sampling attention module (SAM), channel attention module (CAM) and elaborate multi-depth residual connection aiming at the essential multi-scale features by up-sampling and down-sampling to leverage the features in CT images. (3) We design a multi-supervised mechanism based on shared task heads, which introducing the denoising head into SR task to concentrate on the connection between the SR task and the denoising task. Such design could suppress more artifacts while decreasing the number of parameters.
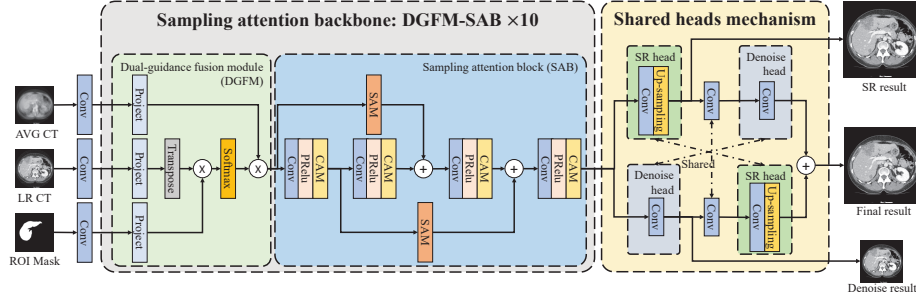
(a) Overall architecture of our LDCT SR network
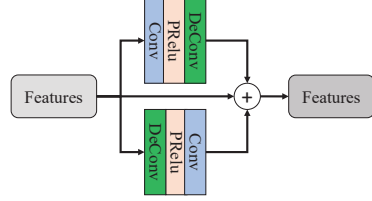
(b) Architecture of sampling attention module (SAM)
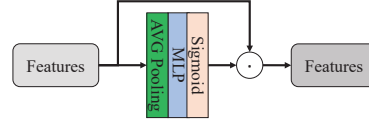
(c) Architecture of channel attention module (CAM)

Fig. 1: Architecture of our proposed method. SAM is sampling attention module. CAM is channel attention module. AVG CT is the average image among adjacent CT slices of each patient.

2 Method

2.1 Overall Architecture

The pipeline of our proposed method is shown in Fig. 1(a). We first calculate the average CT image of adjacent CT slices of each patient to provide the 3D spatial structure information of CT volume. Meanwhile, the ROI mask is obtained by a pre-trained segmentation network to guide the network to concentrate on the focus area or tissue area. Then those guidance images and the input LDCT image are fed to the dual-guidance feature distillation backbone to extract the deep

features. Finally, the proposed dual-path architecture consisting of parameter-shared SR heads and denoising heads leverages the deep visual features obtained by our backbone to build the connection between the SR task and the denoising task, resulting in noise-free and detail-clear reconstructed results.

Dual-guidance feature distillation Backbone To decrease the redundant computation and make full use of the above-mentioned extra information, we design a dual-guidance feature distillation backbone consisting of a dual-guidance fusion module (DGFM) and sampling attention block(SAB).

Firstly, we use a 3×3 convolutional layer to extract the shallow features of the three input images. Then, those features are fed into 10 DGFM-SAB blocks to obtain the deep visual features.

Especially, the DGFM-SAB block is composed of DGFM concatenated with SAB. Considering the indicative function of ROI, we calculate the correlation matrix between LDCT and its mask and then acquire the response matrix between the correlation matrix and the average CT image by multi-heads attention mechanism:

$$F_i = Softmax[Prj(F_i^{SAB})^T \times Prj(F_{mask})] \times Prj(F_{AVG}) \qquad (1)$$

where, F_i^{SAB} are the output of i-th SAB. F_{mask} and F_{AVG} represent the shallow features of the input ROI mask and the average CT image respectively. Meanwhile, $Prj(\cdot)$ is the projection function, $Softmax[\cdot]$ means the softmax function and F_i are the output features of the i-th DGFM. The DGFM helps the backbone to focus on the ROI and tiny structural information by continuously introducing additional guidance information.

Furthermore, to take advantage of the multi-scale information which is essential for obtaining the response matrix containing the connections between different levels of features, as shown in Fig. 1(b), we design the sampling attention block (SAB) which introduces the resampling features into middle connection to fuse the multi-scale information. In the SAB, the input features are up-sampled and down-sampled simultaneously and then down-sampled and up-sampled to recover the spatial resolution, which can effectively extract multi-scale features. In addition, as shown in Fig. 1(c), we introduce the channel attention module (CAM) to focus on those channels with high response values, leading to detailed features with high differentiation to different regions.

Shared Heads Mechanism Singly using the SR head that consists of Pixel Shuffle layer and convolution layer fails to suppress the residual artifacts because of its poor noise removal ability. To deal with this problem, we develop a dual-path architecture by introducing the shared denoising head into SR task where the parameters of SR heads and denoising heads in different paths are shared respectively. Two paths are designed to process the deep features extracted from our backbone: (1) The SR path transfers the deep features to those with high-frequency information and reconstructs the SR result, and (2) the denoising

path migrates the deep features to those without noise and recovers the clean result secondly. Especially, the parameters of those two paths are shared and optimized by multiple supervised strategy simultaneously. This process could be formulated as:

$$I_{final} = \frac{I_{f1} + I_{f2}}{2} = \frac{DN[H_{3\times3}(I_{SR})] + SR[H_{3\times3}(I_{DN})]}{2}$$
$$= \frac{H_{1\times1}\langle H_{3\times3}\{PS[H_{3\times3}(F_n)]\}\rangle + PS\langle H_{3\times3}\{H_{3\times3}[H_{1\times1}(F_n)]\}\rangle}{2} \quad (2)$$

where, F_n is the output of our backbone, $H_{k\times k}$ means $k \times k$ convolutional layer, $SR(\cdot)$ represents SR head, $DN(\cdot)$ represents denoising head, $PS(\cdot)$ expresses Pixel Shuffle layer, I_{SR} is the result of SR head, I_{DN} is the result of denoising head and I_{final} is the final reconstructed result.

2.2   Target Function

Following the multiple supervision strategy, the target function L_{total} is calculated as:

$$L_{total} = \lambda_1 L_{SR} + \lambda_2 L_{DN} + L_{final}$$
$$= \lambda_1 \|I_{gt} - I_{SR}\|_1 + \lambda_2 \|BI(I_{gt}) - I_{DN}\|_1 + \|I_{gt} - I_{final}\|_1 \quad (3)$$

where, I_{gt} is the ground truth, $BI(\cdot)$ means bicubic interpolation, $\|\cdot\|_1$ represents the L1 norm and λ_1, λ_2 are the weight parameters for adjusting the losses.

3   Experiments

3.1   Datasets and Experiment Setup

Datasets Two widely-used public CT image datasets, 3D-IRCADB [5] and PANCREAS [5], are used for both training and testing. The 3D-IRCADB dataset is used for liver and its lesion detection which consists of 2823 512×512 CT files from 20 patients. We choose 1663 CT images from 16 patients for training, 226 CT images from 2 patients for validation and 185 CT images from 2 patients for testing. Similarly, the PANCREAS dataset is used for pancreas segmentation which consists of 19328 512×512 CT files from 82 patients. We choose 5638 CT images from 65 patients for training, 668 CT images from 8 patients for validation and 753 CT images from 9 patients for testing. All HU values are set as [-135, 215]. Following Zeng et al. [30], we set the blank flux as 0.5×10^5 to simulate the effect of low dose noise. And we use bicubic interpolation to degrade the HR images to 256×256 LR images and 128×128 LR images.

Table 1: Ablation experiments on PANCREAS dataset with the scale factor of 2 and 4

(a) Ablation experiments for dual-guidance on the PANCREAS dataset with the scale factor of 2 and 4

AVG CT	Mask	×2		×4	
		PSNR	SSIM	PSNR	SSIM
×	×	30.0282 ± 2.9426	0.8948 ± 0.0431	28.5120 ± 2.2875	$\underline{0.8643} \pm 0.0508$
✓	×	29.9600 ± 3.2378	0.8950 ± 0.0419	28.1490 ± 2.3284	0.8592 ± 0.0543
×	✓	$\underline{30.2991} \pm 3.1391$	$\underline{0.8960} \pm 0.0413$	$\underline{28.6589} \pm 2.2497$	0.8639 ± 0.0522
✓	✓	$\mathbf{30.4047} \pm 3.1558$	$\mathbf{0.8974} \pm 0.0383$	$\mathbf{28.7542} \pm 2.2728$	$\mathbf{0.8672} \pm 0.0412$

The best quantitative performance is shown in **bold** and the second-best in underlined.

(b) Ablation experiments for shared heads mechanism on the PANCREAS dataset with the scale factor of 2 and 4

Heads	Param (M) ×2/×4	×2		×4	
		PSNR	SSIM	PSNR	SSIM
SR Only	5.748/5.896	30.2904 ± 3.0620	$\underline{0.8948} \pm 0.0431$	28.4422 ± 2.3707	0.8628 ± 0.0523
Unshared	6.009/6.304	$\underline{30.3257} \pm 3.2504$	0.8940 ± 0.0442	$\underline{28.5675} \pm 2.2540$	$\underline{0.8645} \pm 0.0529$
Shared	5.795/5.934	$\mathbf{30.4047} \pm 3.1558$	$\mathbf{0.8974} \pm 0.0383$	$\mathbf{28.7542} \pm 2.2728$	$\mathbf{0.8672} \pm 0.0412$

Experiment Setup All experiments are implemented on Ubuntu 16.04.12 with an NVIDIA RTX 3090 24G GPU using Pytorch 1.8.0 and CUDA 11.1.74. We augment the data by rotation and flipping first and then randomly crop them to 128×128 patches. Adam optimizer with $\beta_1 = 0.9$ and $\beta_2 = 0.99$ is used to minimize the target function. λ_1 and λ_2 of our target function are set as 0.2. The batch size is set to 16 and the learning rate is set to 10^{-4} which decreases to 5×10^{-5} at 200K iterations. Peak signal-to-noise (PSNR) and structural similarity (SSIM) are used as the quantitative indexes to evaluate the performance.

3.2   Ablation Study

Table 1a shows the experimental result of the dual-guidance ablation study. Introducing the average CT image guidance alone degrades performance compared with the model without guidance for both the scale factor of 2 and 4. And introducing mask guidance alone could improve the reconstruction effect. When the average CT image guidance and the mask guidance are both embedded, the performance will be promoted further. Table 1b presents the result of the shared heads mechanism ablation study. The experimental result proves that introducing the proposed dual-path architecture could promote the reconstruction performance and the model with shared heads is superior than that without them in both reconstruction ability and parameter amount.

3.3   Comparison with State-of-the-art Methods

We compare the performance of our proposed method with other state-of-the-art methods, including Bicubic interpolation [16], DAN [11], RealSR [15], SPSR [21], AID-SRGAN [12] and JDNSR [10].

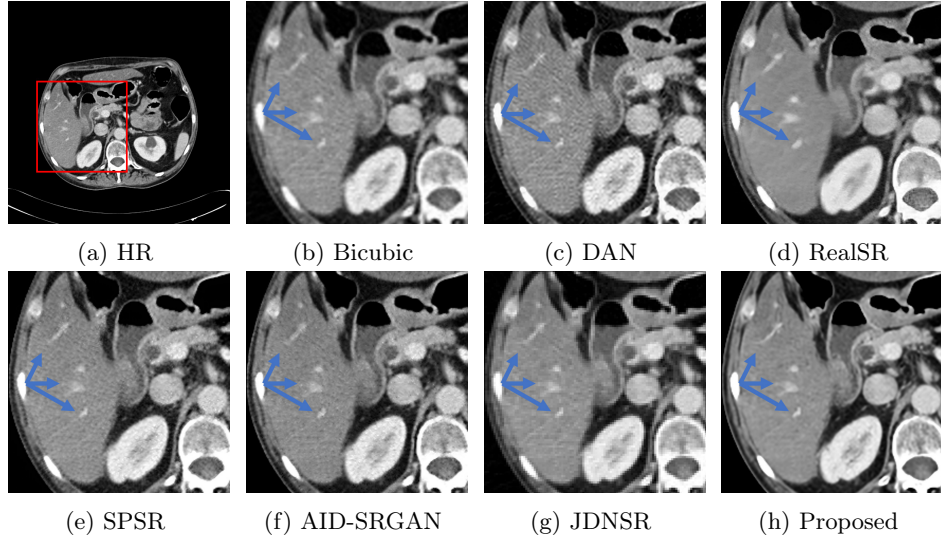|			
(a) HR	(b) Bicubic	(c) DAN	(d) RealSR
(e) SPSR	(f) AID-SRGAN	(g) JDNSR	(h) Proposed

Fig. 2: Qualitative results on the 3D-IRCADB dataset with the scale factor of 2. (a) is the HR image and its red rectangle region displays the liver and its lateral issues. (b) to (h) are the reconstruction results by different methods.

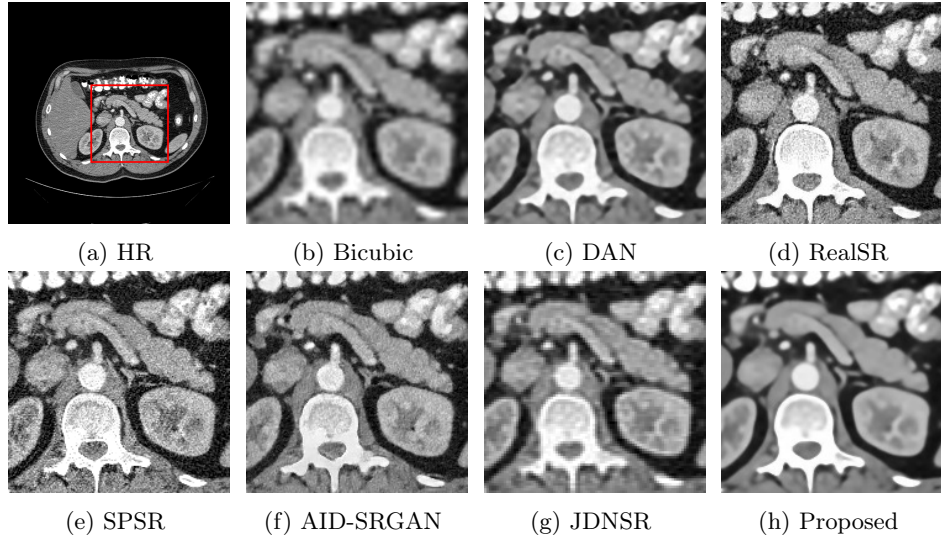|			
(a) HR	(b) Bicubic	(c) DAN	(d) RealSR
(e) SPSR	(f) AID-SRGAN	(g) JDNSR	(h) Proposed

Fig. 3: Qualitative results on PANCREAS dataset with the scale factor of 4. (a) is the HR image and its red rectangle region shows the pancreas and kidney. (b) to (h) are the reconstruction results by different methods.

Fig. 2 shows the qualitative comparison results on the 3D-IRCADB dataset with the scale factor of 2. All methods enhance the image quality to different ex-

Table 2: Quantitative comparison on the 3D-IRCADB and PANCREAS datasets with other state-of-the-art methods

Method	Scale	3D-IRCADB		PANCREAS	
		PSNR↑	SSIM↑	PSNR↑	SSIM↑
Bicubic	2	28.2978 ± 1.0071	0.8613 ± 0.0400	26.9997 ± 1.7192	0.8362 ± 0.0452
DAN	2	29.4768 ± 1.7852	0.8636 ± 0.0465	28.1050 ± 2.8794	0.8602 ± 0.0510
RealSR	2	<u>30.0746</u> ± 1.6303	<u>0.8981</u> ± 0.0390	<u>28.6712</u> ± 2.8363	<u>0.8784</u> ± 0.4810
SPSR	2	29.8686 ± 1.8197	0.8809 ± 0.0417	28.3321 ± 2.9872	0.8755 ± 0.0508
AID-SRGAN	2	29.6212 ± 1.5741	0.8784 ± 0.0423	27.5311 ± 2.7042	0.8579 ± 0.0521
JDNSR	2	27.7927 ± 0.9000	0.8579 ± 0.0402	25.7842 ± 1.7106	0.8322 ± 0.0424
Proposed	2	**31.7642** ± 2.5292	**0.9138** ± 0.0362	**30.4047** ± 3.1558	**0.8974** ± 0.0383
Bicubic	4	25.9209 ± 0.5327	0.8071 ± 0.0452	23.7091 ± 1.4903	0.7700 ± 0.5860
DAN	4	<u>29.4389</u> ± 1.6800	<u>0.8703</u> ± 0.0471	<u>27.5829</u> ± 2.4628	<u>0.8491</u> ± 0.0534
RealSR	4	27.5951 ± 0.9666	0.8272 ± 0.0508	25.9374 ± 2.0109	0.8214 ± 0.0621
SPSR	4	25.8575 ± 0.5969	0.7948 ± 0.0544	25.5834 ± 2.3017	0.8105 ± 0.0675
AID-SRGAN	4	27.5824 ± 1.1192	0.8312 ± 0.0506	26.0488 ± 1.9642	0.8193 ± 0.0585
JDNSR	4	26.6793 ± 0.6690	0.8194 ± 0.0438	24.7504 ± 1.4858	0.7857 ± 0.0515
Proposed	4	**30.0436** ± 1.7803	**0.8811** ± 0.462	**28.7542** ± 2.2728	**0.8672** ± 0.0412

tents compared with bicubic interpolation. However, for the calcifications within the liver which are indicated by the blue arrows, our method recovers the clearest edges. The results of DAN, SPSR and AID-SRGAN suffers from the artifacts. JDNSR blurs the issue structural information, e.g. the edges of liver and bone. For the inferior vena cava, portal vein, and gallbladder within the kidney, RealSR restores blurred details and textures though it could recover clear edges of calcifications. Fig. 3 shows the qualitative comparison results on the PANCREAS dataset with the scale factor of 4. Fig. 3 has similar observation as Fig. 2, that is, our method could suppress more artifacts than other methods, especially at the edges of the pancreas and the texture and structure of the issues with in the kidney. Therefore, our method reconstructs more detailed results than other methods.

Table 2 shows the quantitative comparison results of different state-of-the-art methods with two scale factors on two datasets. For the 3D-IRCADB and PAN-CREAS datasets, our method outperforms the second-best methods 1.6896/0.0157 and 1.7325/0.0187 on PSNR/SSIM with the scale factor of 2 respectively. Similarly, our method outperforms the second-best methods 0.6047/0.0157 and 1.1813/0.0281 on PSNR/SSIM with the scale factor of 4 respectively. Those quantitative superiorities confirm our qualitative observations.

4   Conclusion

In this paper, we propose an LDCT image SR network with dual-guidance feature distillation and dual-path content communication. Facing the existing problem that reconstructed results suffer from residual artifacts, we design a dual-guidance feature distillation backbone which consists of DGFM and SAB to extract deep visual information. Especially, the DGFM could fuse the average CT image to take the advantage of the 3D spatial information of CT volume and the segmentation mask to focus on the ROI, which provides pixel-wise shallow

information and deep semantic features for our backbone. The SAB leverages the essential multi-scale features to enhance the ability for feature extraction. Then, our shared heads mechanism reconstructs the deep features obtained by our backbone to satisfactory results. The experiments compared with 6 state-of-the-art methods on 2 public datasets demonstrate the superiority of our method.

References

1. Bruno, D.M., Samit, B.: Distance-driven projection and backprojection in three dimensions. Physics in Medicine and Biology **49**(11), 2463–2475 (June 2004)
2. Chen, H., Zhang, Y., Kalra, M.K., Lin, F., Chen, Y., Liao, P., Zhou, J., Wang, G.: Low-dose ct with a residual encoder-decoder convolutional neural network. IEEE transactions on medical imaging **36**(12), 2524–2535 (2017)
3. Chen, Y., Zheng, Q., Chen, J.: Double paths network with residual information distillation for improving lung ct image super resolution. Biomedical Signal Processing and Control **73**, 103412 (2022)
4. Chi, J., Sun, Z., Wang, H., Lyu, P., Yu, X., Wu, C.: Ct image super-resolution reconstruction based on global hybrid attention. Computers in Biology and Medicine **150**, 106112 (2022)
5. Clark, K., Vendt, B., Smith, K., Freymann, J., Kirby, J., Koppel, P., Moore, S., Phillips, S., Maffitt, D., Pringle, M., et al.: The cancer imaging archive (tcia): maintaining and operating a public information repository. Journal of digital imaging **26**(6), 1045–1057 (2013)
6. Dai, T., Cai, J., Zhang, Y., Xia, S.T., Zhang, L.: Second-order attention network for single image super-resolution. In: Proceedings of the IEEE/CVF conference on computer vision and pattern recognition. pp. 11065–11074 (2019)
7. Dong, C., Loy, C.C., He, K., Tang, X.: Learning a deep convolutional network for image super-resolution. In: Computer Vision–ECCV 2014: 13th European Conference, Zurich, Switzerland, September 6-12, 2014, Proceedings, Part IV 13. pp. 184–199. Springer (2014)
8. Dong, C., Loy, C.C., He, K., Tang, X.: Image super-resolution using deep convolutional networks. IEEE transactions on pattern analysis and machine intelligence **38**(2), 295–307 (2015)
9. Dong, C., Loy, C.C., Tang, X.: Accelerating the super-resolution convolutional neural network. In: Computer Vision–ECCV 2016: 14th European Conference, Amsterdam, The Netherlands, October 11-14, 2016, Proceedings, Part II 14. pp. 391–407. Springer (2016)
10. Hou, H., Jin, Q., Zhang, G., Li, Z.: Ct image quality enhancement via a dual-channel neural network with jointing denoising and super-resolution. Neurocomputing **492**, 343–352 (2022)
11. Huang, Y., Li, S., Wang, L., Tan, T., et al.: Unfolding the alternating optimization for blind super resolution. Advances in Neural Information Processing Systems **33**, 5632–5643 (2020)

12. Huang, Y., Wang, Q., Omachi, S.: Rethinking degradation: Radiograph super-resolution via aid-srgan. In: International Workshop on Machine Learning in Medical Imaging. pp. 43–52. Springer (2022)
13. Irani, M., Peleg, S.: Super resolution from image sequences. In: [1990] Proceedings. 10th International Conference on Pattern Recognition. vol. 2, pp. 115–120. IEEE (1990)
14. Irani, M., Peleg, S.: Improving resolution by image registration. CVGIP: Graphical models and image processing **53**(3), 231–239 (1991)
15. Ji, X., Cao, Y., Tai, Y., Wang, C., Li, J., Huang, F.: Real-world super-resolution via kernel estimation and noise injection. In: proceedings of the IEEE/CVF conference on computer vision and pattern recognition workshops. pp. 466–467 (2020)
16. Keys, R.: Cubic convolution interpolation for digital image processing. IEEE transactions on acoustics, speech, and signal processing **29**(6), 1153–1160 (1981)
17. Kim, J., Lee, J.K., Lee, K.M.: Accurate image super-resolution using very deep convolutional networks. In: Proceedings of the IEEE conference on computer vision and pattern recognition. pp. 1646–1654 (2016)
18. Li, B., Li, X., Wang, Y., Han, Y., Wang, Y., Wang, C., Zhang, G., Jin, J., Jia, H., Fan, F., et al.: Diagnostic value and key features of computed tomography in coronavirus disease 2019. Emerging microbes & infections **9**(1), 787–793 (2020)
19. Liang, J., Cao, J., Sun, G., Zhang, K., Van Gool, L., Timofte, R.: Swinir: Image restoration using swin transformer. In: Proceedings of the IEEE/CVF International Conference on Computer Vision. pp. 1833–1844 (2021)
20. Lim, B., Son, S., Kim, H., Nah, S., Mu Lee, K.: Enhanced deep residual networks for single image super-resolution. In: Proceedings of the IEEE conference on computer vision and pattern recognition workshops. pp. 136–144 (2017)
21. Ma, C., Rao, Y., Lu, J., Zhou, J.: Structure-preserving image super-resolution. IEEE Transactions on Pattern Analysis and Machine Intelligence (2021)
22. Prasad, K., Cole, W., Haase, G.: Radiation protection in humans: extending the concept of as low as reasonably achievable (alara) from dose to biological damage. The British journal of radiology **77**(914), 97–99 (2004)
23. Ramani, S., Fessler, J.A.: A splitting-based iterative algorithm for accelerated statistical x-ray ct reconstruction. IEEE Transactions on Medical Imaging **31**(3), 677–688 (2012)
24. Schultz, R.R., Stevenson, R.L.: Extraction of high-resolution frames from video sequences. IEEE transactions on image processing **5**(6), 996–1011 (1996)
25. Smith, P.: Bilinear interpolation of digital images. Ultramicroscopy **6**(2), 201–204 (1981)
26. Stark, H., Oskoui, P.: High-resolution image recovery from image-plane arrays, using convex projections. JOSA A **6**(11), 1715–1726 (1989)
27. Sun, K., Xiao, B., Liu, D., Wang, J.: Deep high-resolution representation learning for human pose estimation. In: Proceedings of the IEEE/CVF conference on computer vision and pattern recognition. pp. 5693–5703 (2019)
28. Veronesi, G., Baldwin, D.R., Henschke, C.I., Ghislandi, S., Iavicoli, S., Oudkerk, M., De Koning, H.J., Shemesh, J., Field, J.K., Zulueta, J.J., et al.: Recommendations for implementing lung cancer screening with low-dose computed tomography in europe. Cancers **12**(6), 1672 (2020)
29. Yin, X., Zhao, Q., Liu, J., Yang, W., Yang, J., Quan, G., Chen, Y., Shu, H., Luo, L., Coatrieux, J.L.: Domain progressive 3d residual convolution network to improve low-dose ct imaging. IEEE transactions on medical imaging **38**(12), 2903–2913 (2019)

30. Zeng, D., Huang, J., Bian, Z., Niu, S., Zhang, H., Feng, Q., Liang, Z., Ma, J.: A simple low-dose x-ray ct simulation from high-dose scan. IEEE transactions on nuclear science **62**(5), 2226–2233 (2015)
31. Zhang, Y., Li, K., Li, K., Wang, L., Zhong, B., Fu, Y.: Image super-resolution using very deep residual channel attention networks. In: Proceedings of the European conference on computer vision (ECCV). pp. 286–301 (2018)
32. Zhang, Y., Tian, Y., Kong, Y., Zhong, B., Fu, Y.: Residual dense network for image restoration. IEEE Transactions on Pattern Analysis and Machine Intelligence **43**(7), 2480–2495 (2020)